nature research

https://doi.org/10.1038/s41563-020-0775-8

Supplementary information

Self-supported Pt–CoO networks combining high specific activity with high surface area for oxygen reduction

In the format provided by the authors and unedited

Supporting information

Self-supported Pt-CoO networks combining high specific activity with high surface area for oxygen reduction

Gustav W. Sievers[a,b], Anders W. Jensen[a], Jonathan Quinson[a], Alessandro Zana[a,c], Francesco Bizzotto[c], Mehtap Oezaslan[d,e], Alexandra Dworzak[d,e], Jacob J. K. Kirkensgaard[f,g], Thomas E. L. Smitshuysen[h], Shima Kadkhodazadeh[h], Mikkel Juelsholt[a] , Kirsten M. Ø. Jensen[a], Kirsten Anklam[b], Hao Wan[a], Jan Schäfer[b], Klára Čépe[i], María Escudero-Escribano[a], Jan Rossmeisl[a], Antje Quade[b], Volker Brüser[b], Matthias Arenz [a,c]

[a] Department of Chemistry, University of Copenhagen, Universitetsparken 5, DK-2100 Copenhagen Ø Denmark

[b] Leibniz Institute for Plasma Science and Technology, Felix-Hausdorff-Strasse 2, 17489 Greifswald, Germany

[c] Department of Chemistry and Biochemistry, University of Bern, Freiestrasse 3, CH-3012 Bern, Switzerland

[d] Department of Chemistry, School of Mathematics and Science, Carl von Ossietzky University of Oldenburg, 26111 Oldenburg, Germany

[e] Institute of Technical Chemistry, Technische Universität Braunschweig, D-38106 Braunschweig, Germany

[f] Niels Bohr Institute, University of Copenhagen, Universitetsparken 5, DK-2100 Copenhagen, Denmark

[g] Department of Food Science, University of Copenhagen, Rolighedsvej 30, DK-1958 Frederiksberg C, Denmark

[h] Technical University of Denmark, Anker Engelunds Vej 1, 2800 Lyngby, Denmark

[i] Regional Centre of Advanced Technologies and Materials, Šlechtitelů 27, 783 71 Olomouc, Czech Republic

Corresponding author: matthias.arenz@dcb.unibe.ch; sievers@inp-greifswald.de

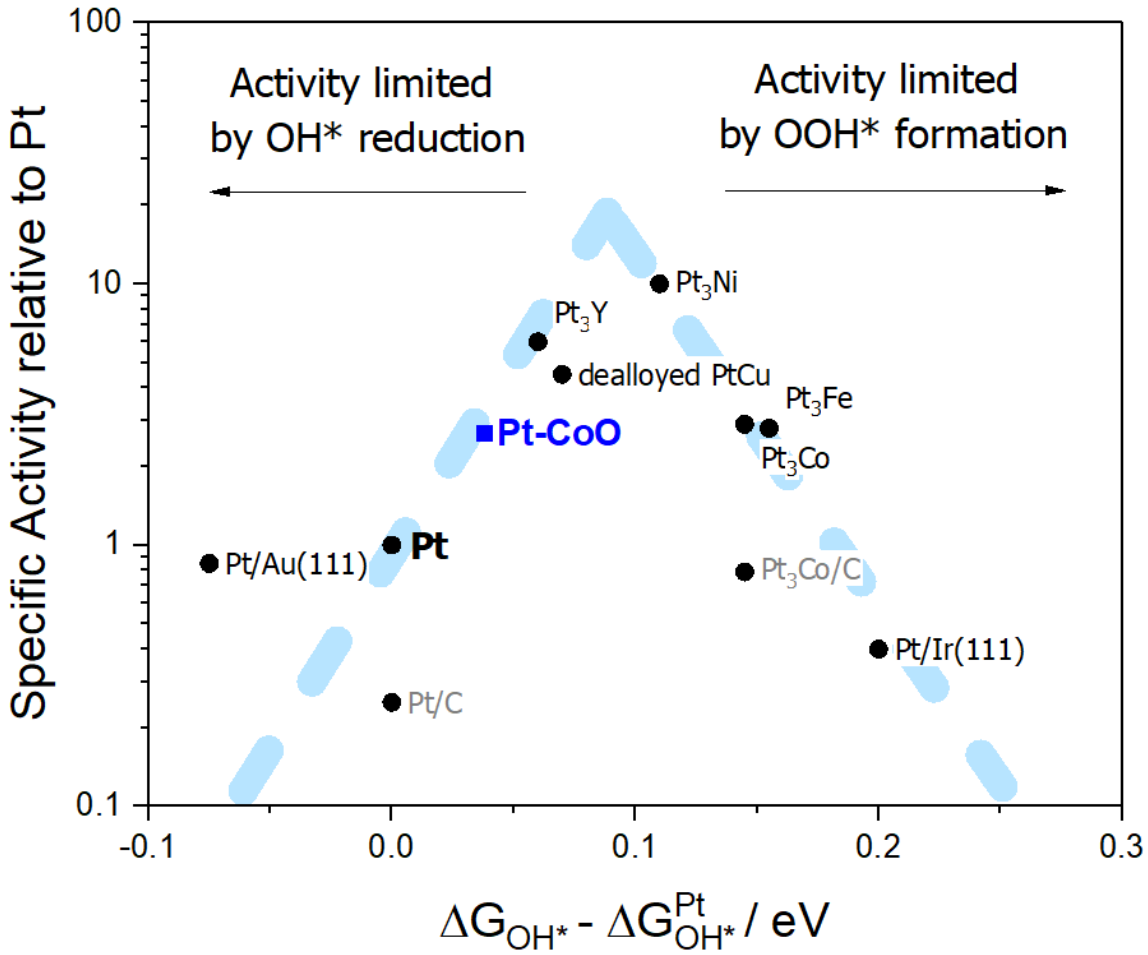

Figure S1. Volcano Plot showing experimental activity data from electrochemical RDE measurements @0.9 V_{RHE} relative to Pt as a function of the hydroxyl intermediate binding energy ΔG_{OH^*}; Data for Pt/Au(111), Pt_3Y, Pt_3Ni, dealloyed PtCu, Pt_3Fe, Pt_3Co and Pt/Ir(111) are taken from Stephens et al.[1] *(black); Data for Pt/C and Pt_3Co/C are as used in this publication assuming the same hydroxyl binding energy as bulk Pt or Pt_3Co respectively (grey); Data for Pt-CoO is taken from DFT calculations and electrochemical activity evaluation.*

Physical and chemical characterization of Pt-CoO networks

The samples were characterized by means of electrochemistry, SEM, EDX, TEM, XPS, SAXS, wide-angle X-Ray scattering and (in and ex situ) XAS see Figures S2 – S23. The nanoporous Pt-CoO films were created by an acid leaching process. The noble metal loading before leaching was determined by ICP-MS to be 22 µg cm^{-2}. The same mass was confirmed by mass gravimetry after magnetron sputtering of pure Pt. In the

leaching process, a porous structure is formed as Cobalt is dissolved. During this leaching process also a considerable amount of Pt is lost to the electrolyte. After leaching the Pt loading was determined by ICP-MS once for each catalyst, see Table S1. All mass activity and surface area calculations are based on the Pt loading after leaching. The remaining Co content was up to 28.4 at. % as measured by EDX. The Co amount was also determined by XPS leading to lower values. This indicates a Co deficiency in the near surface region as expected from the well-known Co leaching.

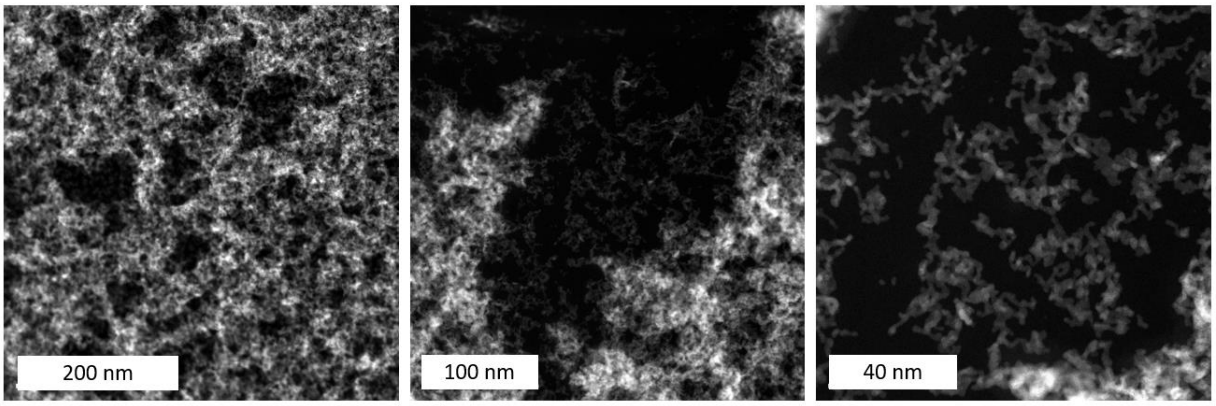

A

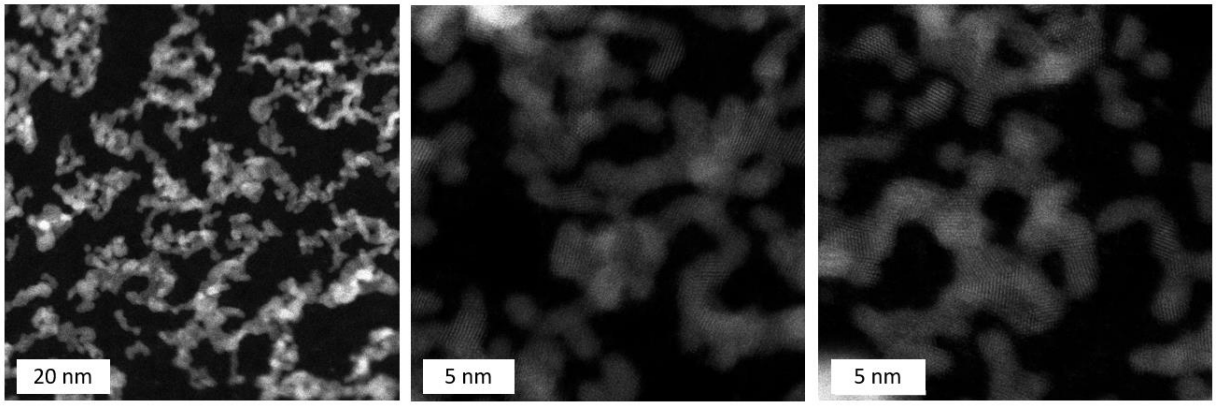

B

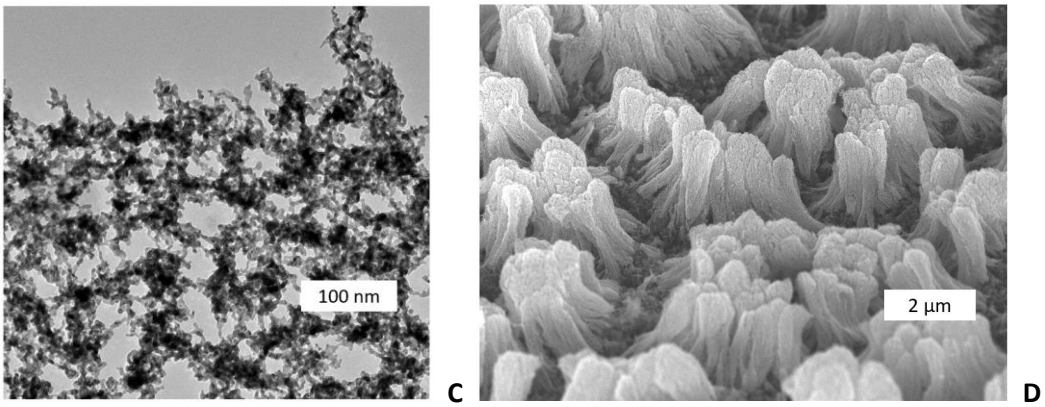

Figure S2. STEM (A, B) and TEM (C) micrographs of Pt-CoO catalyst. D: SEM micrograph of Pt-CoO 2 with a loading of 0.125 mg cm^{-2}_{Pt} on a gas diffusion electrode with microporous layer.

Figure S2 displays representative electron microscope graphs of the leached Pt-CoO catalyst. The bone structure as well as the formation of a nanoporous network are clearly discernable. As a result of the TEM microscopy, we counted 518 bones with an average diameter of 4.0 nm and 694 pores with an average diameter of 15.8 nm (Figures S3 and S4). TEM Tomography calculations show that the mean volume of bone structures is 20.4% (+/- 6.4%) with a standard deviation of the 8 boxes of 6.7 (1.0)%. For the calculations 8 ROI-boxes was made of volumes between 1.2 μm^3 and 1.7 μm^3, see Figure S5. SAXS data (Figure S6) fitting results in a bone diameter of 5.2 nm. The average number determined from the TEM image is lower as we did not count the agglomerates, which are included in the SAXS data.

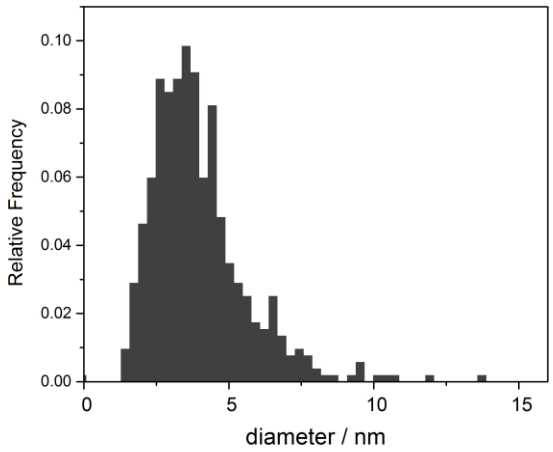

Figure S3. Histogram of TEM bone diameter analysis of the nanoporous Pt-CoO catalyst. The analysis was carried out by measuring bone size with ImageJ. In total 518 bones were measured.

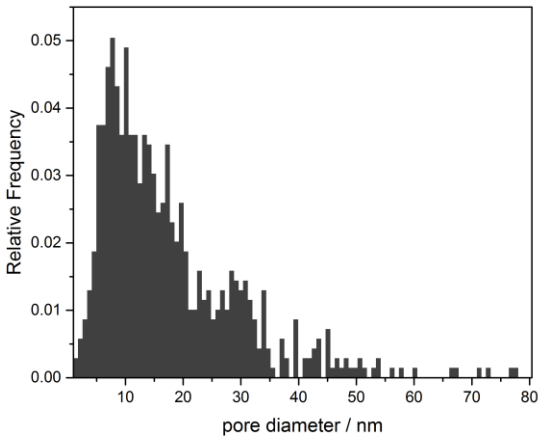

Figure S4. Histogram of TEM pore size analysis of nanoporous Pt-CoO catalyst. The analysis was carried out by measuring pore size with ImageJ. In total 694 pores were measured.

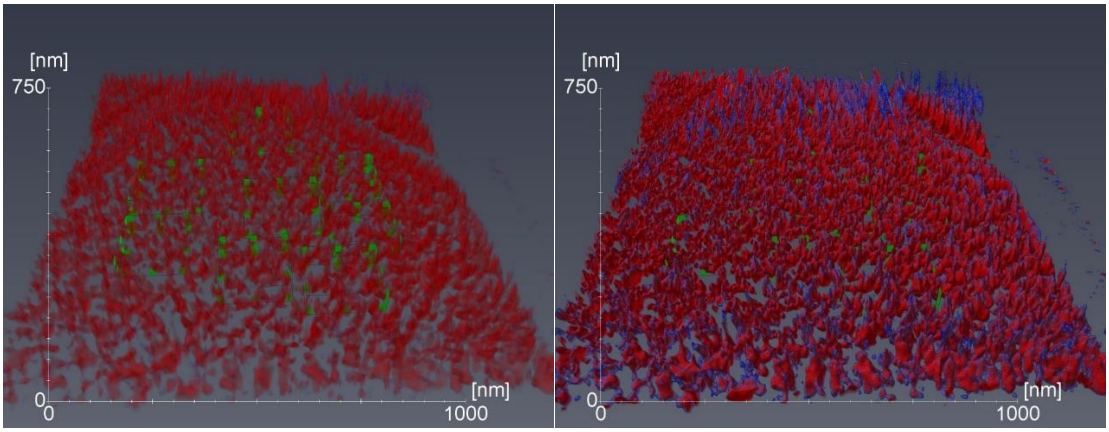

Figure S5. Volume Estimation for the np Pt-CoO network. ROI-boxes (green corners) are made inside the tomogram, iso-surfaces(red surface) within ROI-boxes are triangulated and volumes of the surfaces are estimated. Ratio will be iso-volume over ROI-volume.

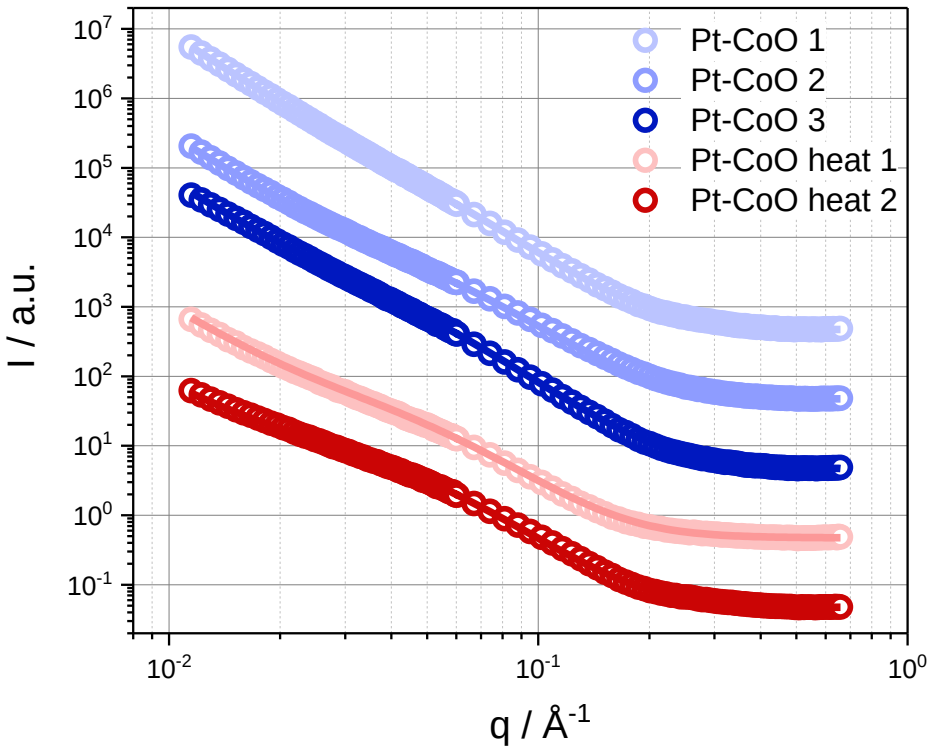

Figure S6. SAXS data of Pt-CoO 1, Pt-CoO 2, Pt-CoO 3, Pt-CoO heat 1 and Pt-CoO heat 2. Scattering data (circles) and corresponding fits (lines), see methods section for details.

The data for EDX and XPS is shown in Figure S7 and S8.

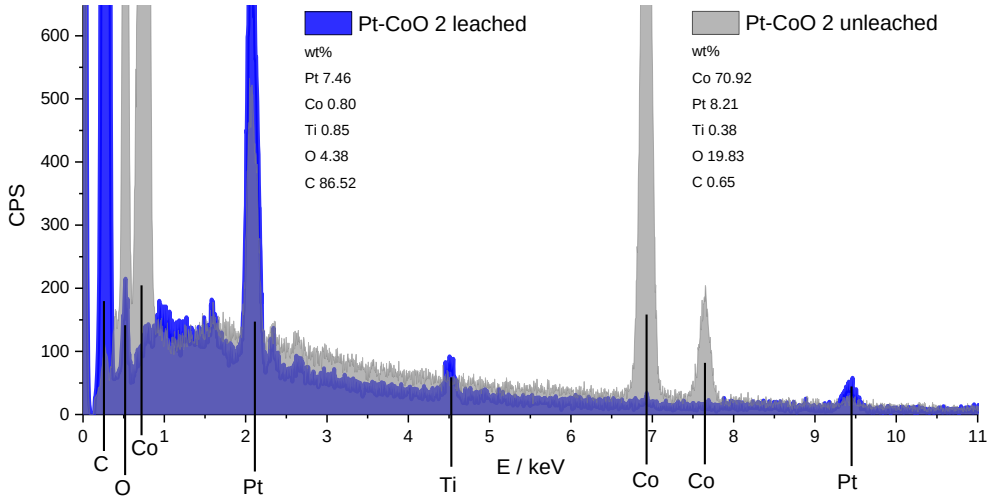

Figure S7. Energy-dispersive X-ray spectroscopy (EDX) of Pt-CoO 2. Comparison between unleached Pt-CoO 2 and leached Pt-CoO 2.

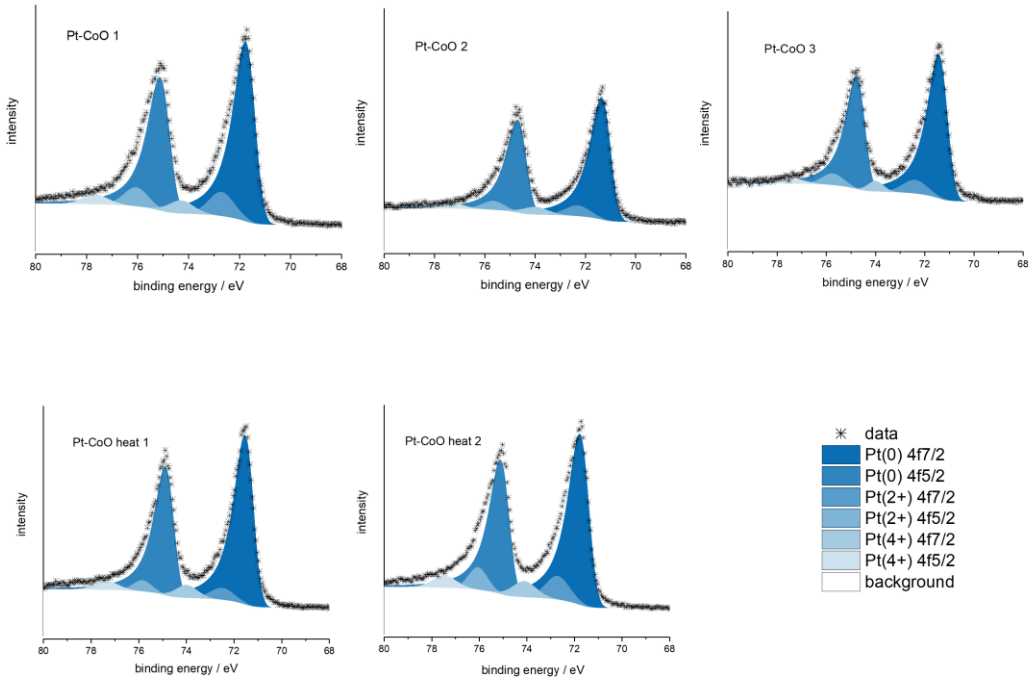

Figure S8. XPS Data and corresponding fits of the individual Pt-CoO samples.

Description of the electrochemical characterization, CV and ECSA determination

Each catalyst was prepared and tested at least 3 times to demonstrate the reproducibility of the synthesis approach. The catalysts were characterized electrochemically in Ar saturated 0.1 M $HClO_4$ electrolyte. The respective sample was cycled until the CV was stable and the electrolyte was changed to remove the Cobalt ions from the solution. Typically, the leaching was completed (as indicated by a stable CV) after cycling once between 0.05 V_{RHE} and 1.1 V_{RHE} in the case of non-heated samples and after up to 5 cycles in the case of heat-treated samples. In order to fully leach the samples, they were cycled 30 times at 100 mV s^{-1}. The Pt features, i.e. the hydrogen under potential deposition (H_{upd}) decreased during the first cycles indicating the total loss of Pt (in addition to the Co) leaching. Based on the CVs and ICP-MS in total up to 58% of the Pt is lost during the electrochemical leaching, see Table S1. For large-scale catalyst synthesis, this should not be a problem as the Pt can be easily recovered and reused.

Table S1. Pt mass measured by ICP-MS after leaching and ORR measurements.

	$\mu g_{Pt}\ cm^{-2}$	**Pt loss%**
Pt-CoO 1	10.13	54%
Pt-CoO 2	10.37	53%
Pt-CoO 3	9.31	58%
Pt-CoO heat 1	9.61	56%
Pt-CoO heat 2	9.29	58%

Thereafter, 10 additional CVs were recorded in Ar saturated 0.1 M $HClO_4$, before purging the electrolyte with oxygen and measuring the ORR in O_2 saturated solution at 1600 rpm, see Figure S9 for an example of a polarization curve. The ORR activity was determined from three different positive going potential scan between 0.05 V_{RHE} and 1.1 V_{RHE} recorded with a scan speed of 50 mV s^{-1} and applying compensation of the internal resistance. The potential scan was corrected for non-ORR contributions by subtraction a corresponding potential scan recorded in Argon saturated electrolyte. A Tafel plot of thus determined ORR activities is shown in Figure S10. For comparison to benchmark catalysts we used the ORR activities at 0.9 V_{RHE} and 0.95 V_{RHE}. 0.9 V_{RHE} is a standard potential, however, as seen from the polarization curves, at such potential very active catalysts almost reach the diffusion limitations. For the calculation of the kinetic activity the Koutecky-Levich equation was used:

$$\frac{1}{i} = \frac{1}{i_k} + \frac{1}{i_{diff}}$$

To calculate i_k one can re-write above formula to:

$$i_k = \frac{i \times i_{diff}}{(i_{diff} - i)}$$

To normalize for the real surface area, the current has to be divided by the roughness factor r_f.

$$j_k(Pt) = \frac{i_k}{r_f \times A_{geo}}$$

For further information, see for example ref. [2]

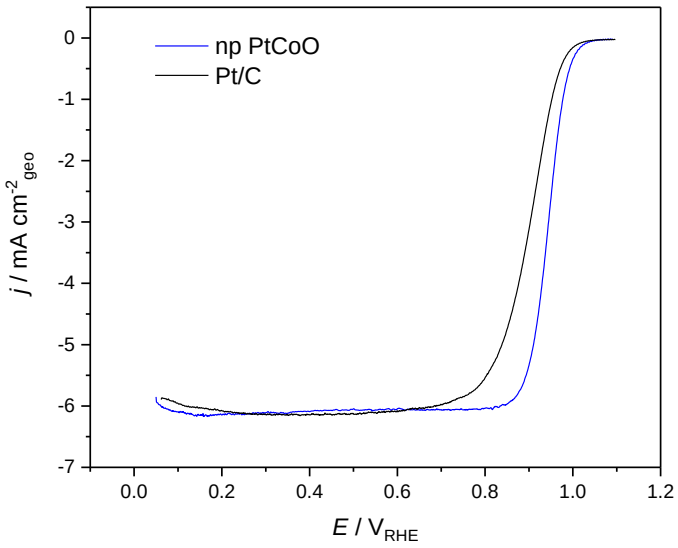

A

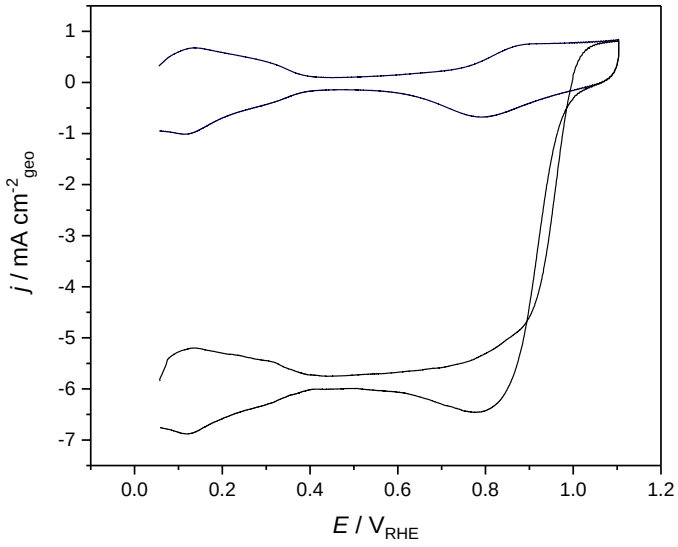

B

Figure S9. A: Oxygen reduction curve for a Pt/C standard (black) and Pt-CoO (blue) measured in 0.1 M $HClO_4$ at 50 mV s^{-1} and 1600 rpm (positive sweep). B: Cyclic voltammetry of Pt-CoO in argon and in oxygen saturated 0.1 M $HClO_4$ at 50 mV s^{-1} and 1600 rpm. *Ohmic resistance was compensated during the experiment and the capacitive background in argon was subtracted from the reduction curve in O_2.*

The mass activity was calculated as:

$$j_{mass} = j_k \times \frac{r_f}{L_{Pt}}$$

where L_{Pt} is the Pt loading. The high specific activity combined with the surface area (roughness factor divided by Pt loading) therefore leads to mass activities of up to 8.37 A mg^{-1}. In Figure S11 we plot the activity as function of the Pt(0) binding energy, demonstrating an increase in activity with higher binding energy.

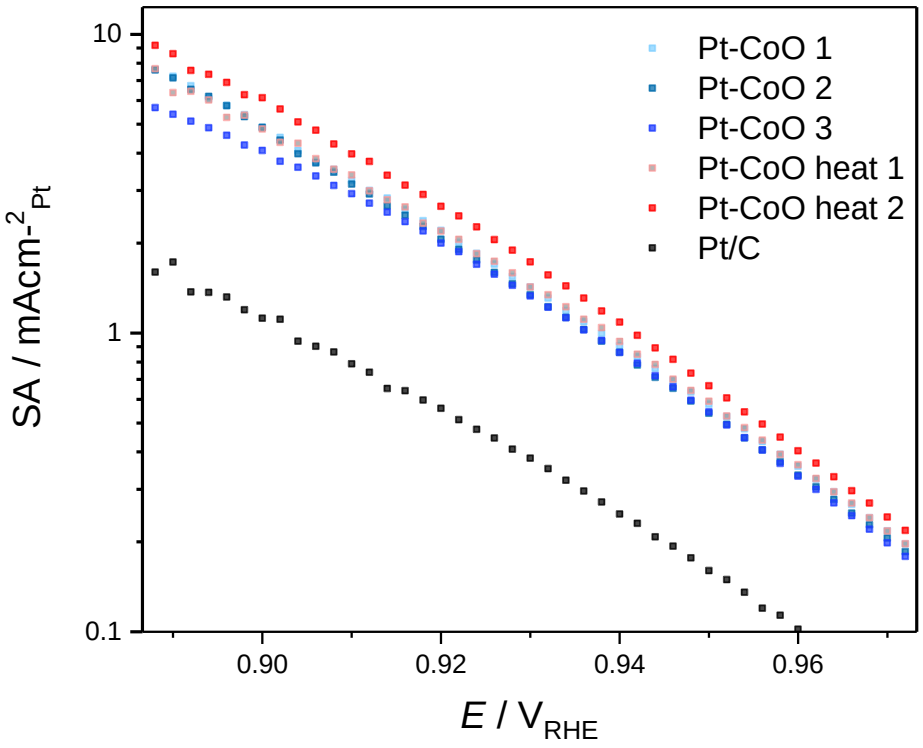

Figure S10. Tafel plots for Pt/C (black) and np Pt-CoO measured in 0.1 M $HClO_4$ at 50 mV s^{-1} and 1600 rpm. The Ohmic resistance was compensated during the experiment, the capacitive background was subtracted from the ORR polarization curve and the current was normalized to the electrochemically active surface area (ECSA) determined in CO stripping measurements.

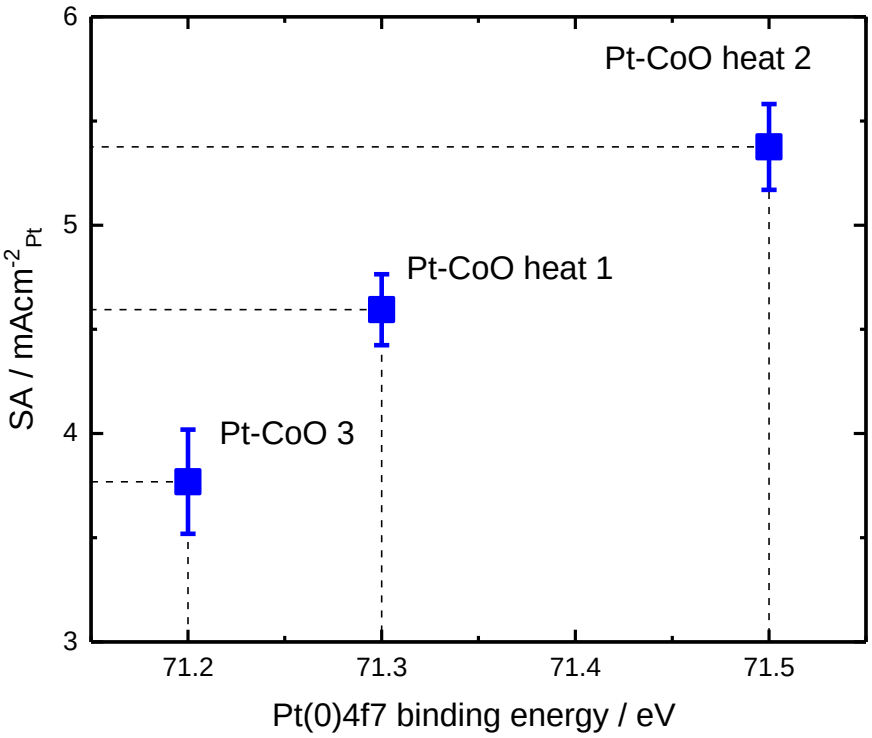

Figure S11. Specific ORR Activity @0.9 V_{RHE} plotted as function of the Pt(0) $4f_{7/2}$ binding energy after heating the sample at 573 K for 8 min (heat 1) or 16 min (heat 2), respectively, followed by rapid cooling (in 8 min) by streaming argon through the chamber.

Following the ORR testing CO stripping was performed to determine the electrochemical Pt surface area (ECSA). In Figure S12, representative CO stripping curves are shown. CO oxidation on the nanoporous Pt-CoO networks is shifted by -150 mV as compared to Pt/C in agreement with "bulk-like" properties. The integrated charge is used for ECSA calculation, see Table 1 and Table S2. The surface area is calculated as Pt surface area (A_{real}) per gram Pt (m):

$$ECSA = \frac{A_{real}}{m} = \frac{r_f \times A_{geo}}{L_{Pt} \times A_{geo}} = \frac{r_f}{L_{Pt}}$$

The Pt loading on the electrode is determined by mass gravimetry and ICP-MS after sputtering and electrochemical testing. ICP-MS measurements confirm that up to 58% of the initial Pt is lost during leaching. For the calculation of the mass activity the specific loading measured by ICP-MS was used.

Table S2. Roughness factor, surface area and mass activity of prepared catalysts.

	Rf CO-Stripping	**Rf H-UPD**	**ECSA CO-Stripping [$m^2g^{-1}_{Pt}$]**	**ECSA H-UPD [$m^2g^{-1}_{Pt}$]**	**MA @0.9V_{RHE} [Amg^{-1}_{Pt}]**
Pt-CoO 1	10.19 ± 0.62	8.6 ± 1.0	101 ± 6	85 ± 10	4.60 ± 0.69
Pt-CoO 2	11.91 ± 0.40	11.5 ± 2.8	115 ± 4	111 ± 28	5.19 ± 0.36
Pt-CoO 3	14.16 ± 1.01	13.7 ± 2.8	152 ± 10	147 ± 28	5.74 ± 0.34
Pt-CoO heat 1	14.11 ± 0.57	12.9 ± 2.5	147 ± 6	134 ± 25	6.75 ± 0.24
Pt-CoO heat 2	14.46 ± 0.43	14.5 ± 2.7	156 ± 4	156 ± 27	8.37 ± 0.30

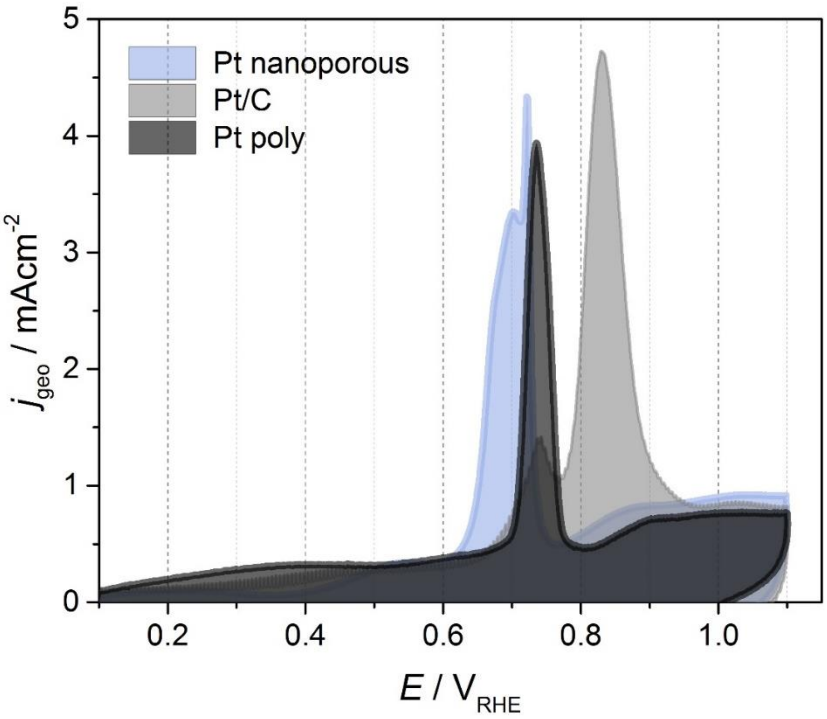

Figure S12. CO stripping curves for Pt-CoO (blue), polycrystalline (poly) Pt (black) and Pt/C (grey). The current density of the polycrystalline Pt polycrystalline is multiplied by a factor of 7 to have a better comparison between the different catalysts.

Stability Measurements at 80 °C in the rotating disc electrode

AST 1 – Load Cycles

The normalized loss of ECSA after the load-cycling treatment between 0.6 V and 1 V was determined to be 47% both by Hupd and CO-stripping as seen in Figure S13. This is in line with the measured loss for the Pt/C catalyst; however, the degradation profile differs substantially. The initial ECSA loss after 600 cycles is substantial, but the further loss between 600 to 3600 cycles is only minor. While high initial ECSA losses are not uncommon, the extensive loss in ECSA observed for the np Pt-CoO catalyst is significantly higher than what normally is accompanying platinum dissolution, where a more linear ECSA decay is expected. It can therefore be speculated that the rapid decrease in ECSA is mainly originating from structural changes – like a partly collapse in the mesoporous structure. In order to get a better insight into the underlying degradation pathway, the catalyst was analyzed with TEM microscopy. TEM images of the microstructure before and after treatment are displayed, see Figure S14. The images show the unique skeleton structure of the catalyst. Furthermore, an average increase in the size of these bones is clearly visible in the degraded sample. This agglomeration on the skeleton bones most likely originated from the dissolution of platinum follow by redeposition on the bones. Thus, the TEM image indicates a surface area loss due to increase in the size of the “bone structure”, but it reveals no sign of changes in the structural morphology. However, it should be noted that TEM is a highly localized technique with poor in-depth resolution, meaning that minor structural alternation would be difficult to identify. Additionally, possible changes in steps and kinks cannot be seen, as the resolution is not high enough.

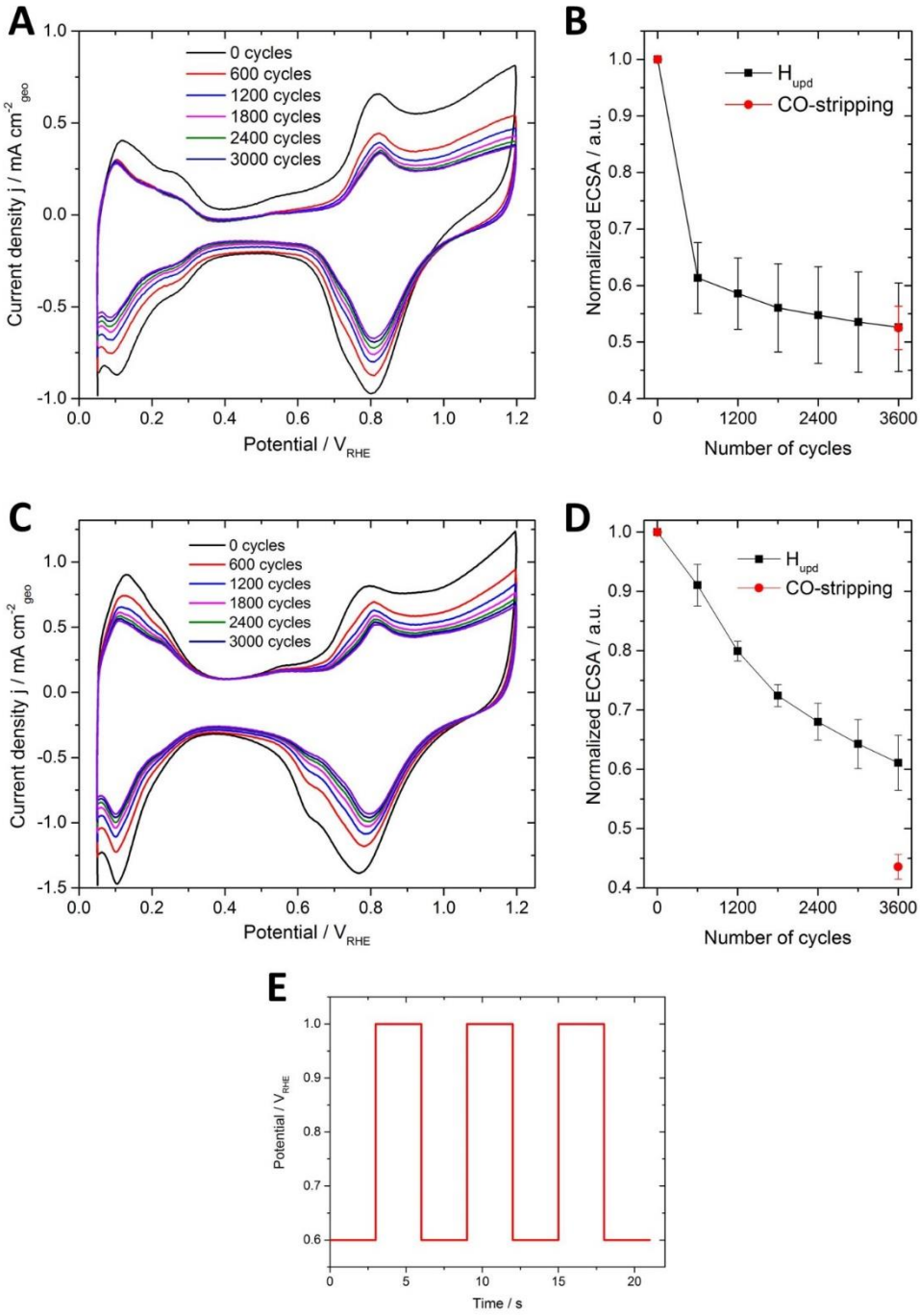

Figure S13. A) Cyclic voltammograms of np Pt-CoO catalyst in Ar saturated 0.1 M $HClO_4$ at 80 ºC during AST 1 treatment, scan rate 50 mV s^{-1}, recorded for every 600 potential sweep cycles between 0.6 and 1.0 V_{RHE} with a Pt loading of 16 μg_{Pt} cm^{-2}B) Normalized ECSA, obtained every 600 cycles from H_{upd} and CO-stripping before and after treatment. C) Cyclic voltammograms of Pt/C (TEC10E50E, 2-3nm) in Ar saturated 0.1 M $HClO_4$ at 80 °C, scan rate 50mV s^{-1}, recorded for every 600 potential sweep cycles between 0.6 and

1.0 V_{RHE} with a Pt loading of 16 μg_{Pt} cm^{-2}. D) Normalized ECSA, obtained every 200 cycles from H_{upd} and CO-stripping before and after treatment. E) Voltage profile during accelerated stress testing. Error bars represent standard deviation based of at least three independent measurements.

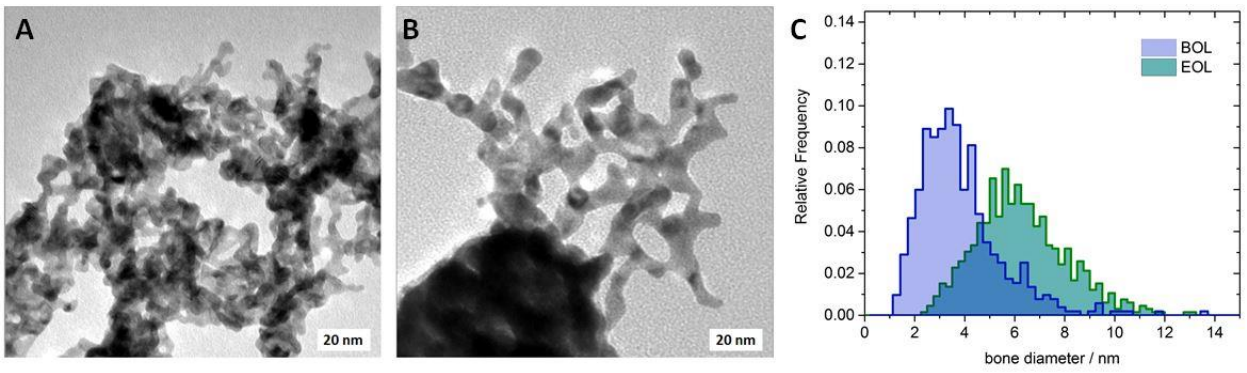

Figure S14. TEM micrographs of the np Pt-CoO catalyst A) before and B) after accelerated stress testing with the load cycle protocol (AST 1) C) Histogram of the bone diameter before and after stability test, for each a minimum of 500 bones were measured.

AST2 – Start Stop Cycles

Start-Stop cycling between 1 V – 1.5 V shows the relative decay of ECSA as observed in Figure S15 revealing a significant improvement in catalyst surface area stability as compared to Pt/C following the AST 2 treatment. A relative loss of only 13% from CO-stripping and 15% for Hupd is observed. The ECSA by Hupd reveals an atypical behavior for the normalized ECSA. Typically, the ECSA decreases during this stress test, as can be seen with Pt/C. It is unusual that with np Pt-CoO the ECSA increases again after 200 cycles. While this observation is within the statistical error, however the trend was observed to different degrees in all three experiments. The TEM microscopy of the sample before and after treatment shown in Figure S16 also demonstrates the lack of enlargement of the skeleton bones as observed during the AST1 treatment.

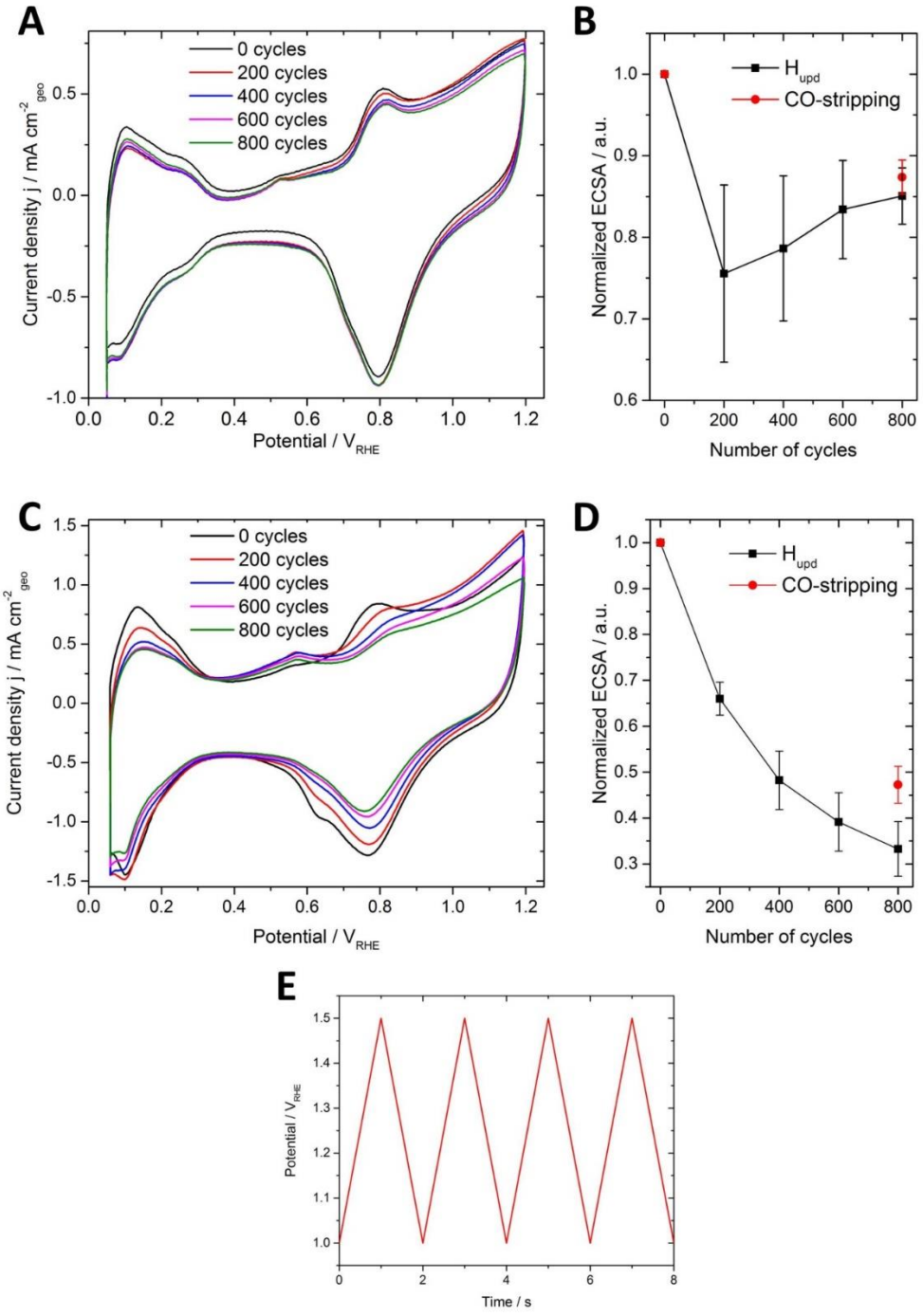

Figure S15. A) Cyclic voltammograms of np Pt-CoO catalyst in Ar saturated 0.1 M $HClO_4$ at 80 °C during Start-Stop cycles (AST 2), scan rate 50 mV s^{-1}, recorded for every 200 potential sweep cycles between 1.0 and 1.5 V_{RHE} with a Pt loading of 16 μg_{Pt} cm^{-2}. B) Normalized ECSA, obtained every 600 cycles from H_{upd} and CO-stripping before and after treatment. C) Cyclic voltammograms of AST2 treated Pt/C (TEC10E50E, 2-

3nm) in Ar saturated 0.1 M $HClO_4$ at 80 °C, scan rate 50 mV s^{-1}, recorded for every 200 potential sweep cycles between 1.0-1.5 V_{RHE} with a Pt loading of 16 μg_{Pt} cm^{-2}. D) Normalized ECSA, obtained every 200 cycles from H_{upd} and CO-stripping before and after treatment. Error bars represent standard deviation based of at least three independent measurements.

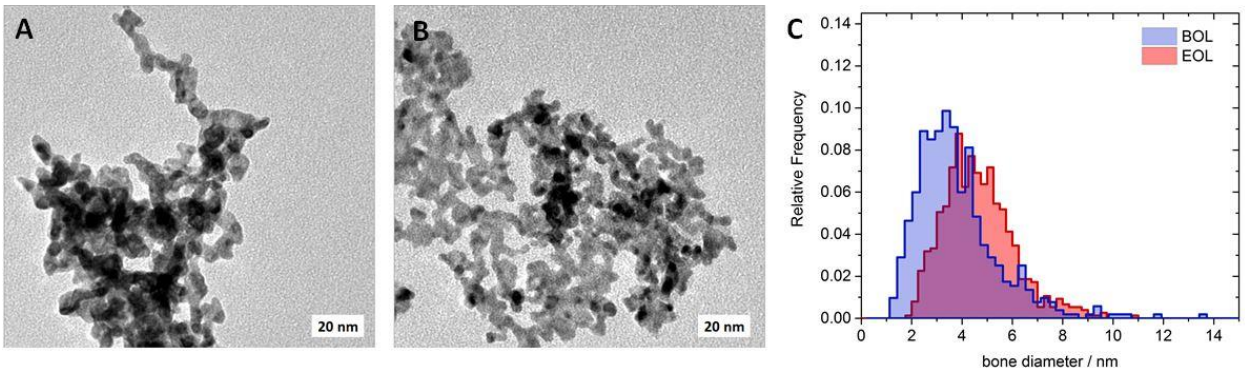

Figure S16. TEM micrographs of the np Pt-CoO catalyst A) before and B) after accelerated stress testing with the start-stop cycle protocol (AST 2) C) Histogram of the bone diameter before and after stability test, for each a minimum of 500 bones were measured.

Specific Activity after accelerated stress testing

The specific activity is decreased significantly from 4.5 to 2.4 mA cm^{-2}_{Pt} after the load cycle stress treatment. After accelerated testing for start-stop conditions the activity was decreased to a specific activity of 3.6 mA cm^{-2}_{Pt} after treatment, see Figure S17.

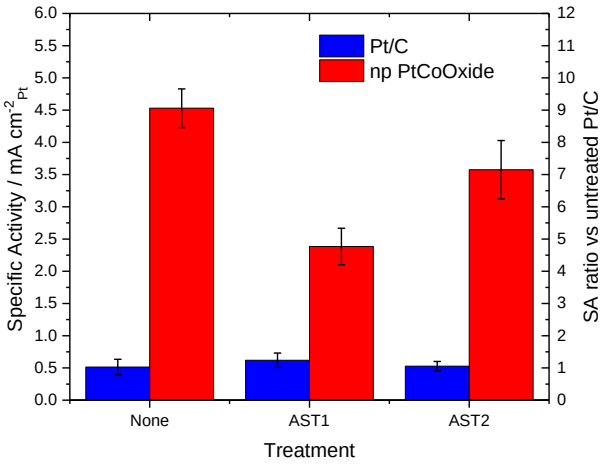

Figure S17. Specific Activity of np Pt-CoO and Pt/C before and after accelerated stress test.

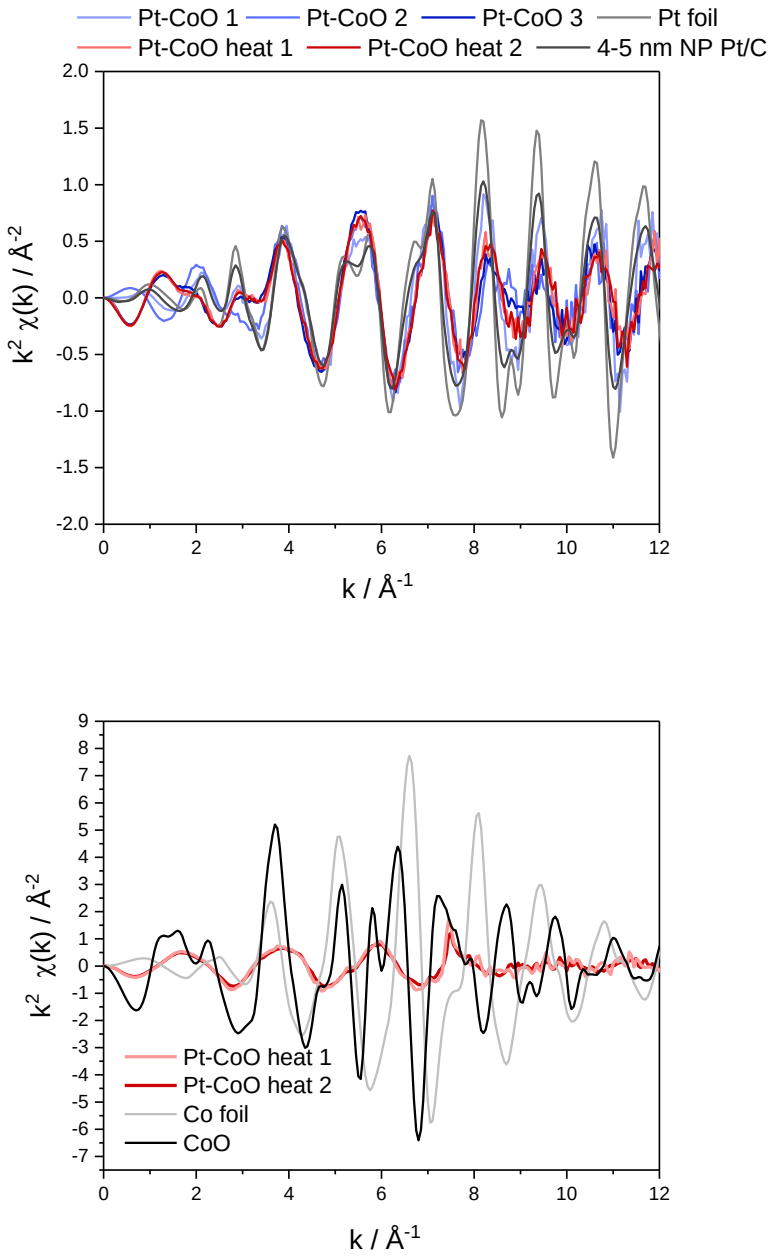

Figure S18. Upper part: k^2-weighted EXAFS data at the Pt L_3 edge for Pt-CoO networks, 4-5 nm Pt NP/C and Pt foil. Lower part: k^2-weighted EXAFS data at the Co K edge for Pt-CoO networks, CoO and Co.

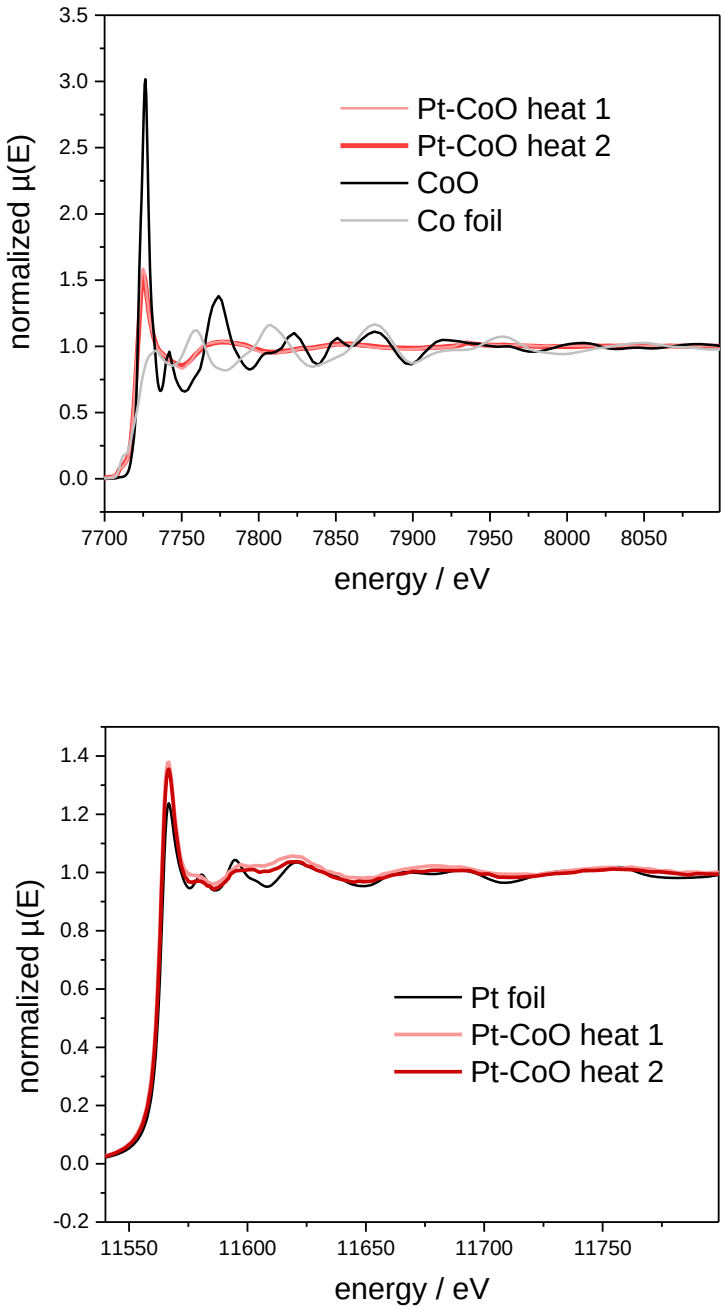

Figure S19. X-ray Absorption Near Edge Structure (XANES) spectra of leached Pt-CoO heat 1, Pt-CoO heat 2 and metallic Pt and Co reference foils at the Co K edge (upper part) and Pt L_3 edge (lower part), indicating that the Co atoms inside the nanoporous Pt network bones are strongly oxidized, while the Pt atoms are only slightly oxidized based on the higher white line intensity.

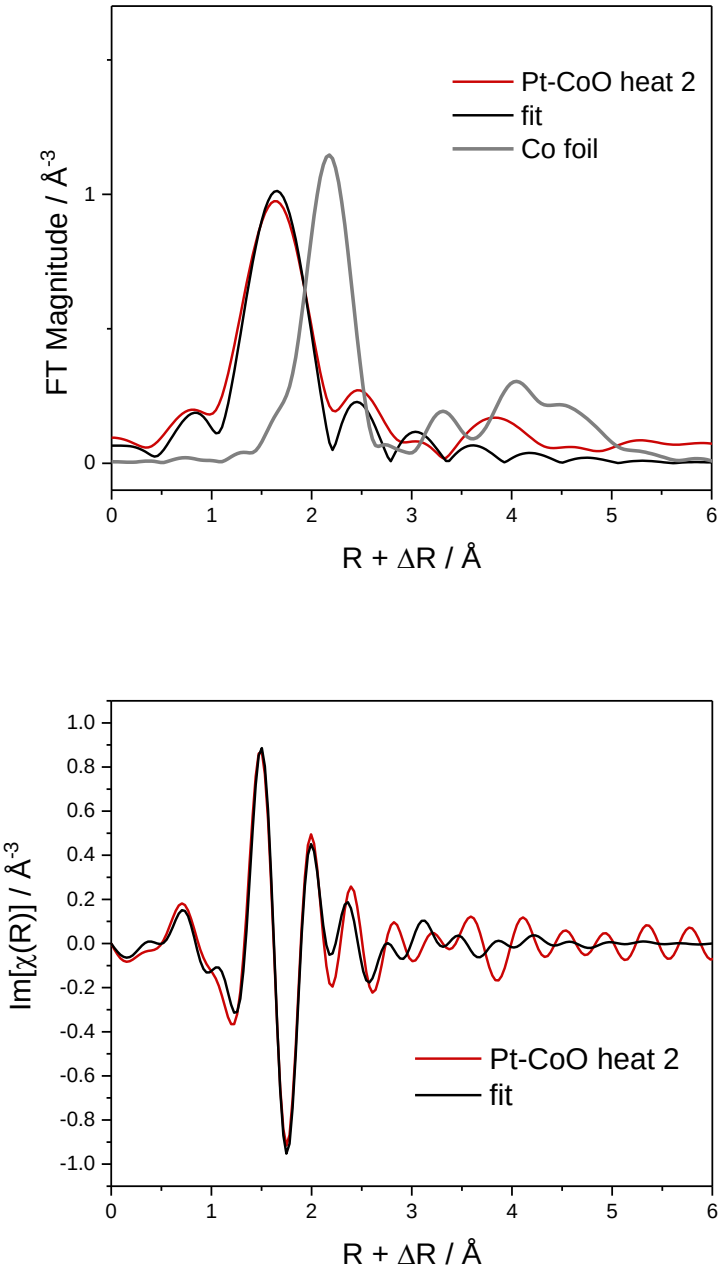

Figure S20. Co K edge Fourier Transform (FT) magnitudes of the k^2-weighted extended X-ray absorption fine structure (EXAFS) data (top) and the imaginary part (bottom) of the FT for the leached nanoporous Pt-CoO networks, see color coding for the individual sample. The data for Co Foil is multiplied by 0.25. The k-ranges for the Fourier-transformed spectra at the Co K edge was from 3 to 9 $Å^{-1}$, while the range for the fit was from 1.1 to 2.9 Å.

Table S3. Pt L_3 edge EXAFS data fitting show first nearest neighbor coordination shell (N), atomic bond length (R), mean squared bond length disorder (σ^2), shift of energy (ΔE_0) at the corresponding edge, and R_f-factor (closeness of the fit as quality parameter) for all Pt-CoO networks, 4-5 nm Pt nanoparticles supported on Carbon and pure Pt foil.

	N	R / Å	σ^2 / 10^{-4} Å	ΔE_0 / eV	R_f
Pt-CoO 1					0.004
Pt-Pt	9.5 ± 1.8	2.731 ± 0.007	56 ± 10	6.8 ± 1.4	
Pt-O	0.8 ± 0.9	2.061 ± 0.077	58 ± 201		
Pt-CoO 2					0.010
Pt-Pt	8.6 ± 3.9	2.728 ± 0.019	116 ± 39	10.2 ± 3.5	
Pt-O	2.4 ± 0.5	2.180 ± 0.018	82 ± 28	17.7 ± 2.7	
Pt-CoO 3					0.006
Pt-Pt	10.7 ± 3.8	2.739 ± 0.019	59 ± 27	10.7 ± 2.5	
Pt-O	2.0 ± 0.5	2.161 ±0.026	15 ± 27	23.2 ± 3.2	
Pt-CoO heat 1					0.011
Pt-Pt	7.8 ± 2.1	2.726 ± 0.015	85 ± 18	7.9 ± 2.6	
Pt-O	2.1 ± 0.7	2.104 ± 0.032	59 ± 43	15.7 ± 3.4	
Pt-CoO heat 2					0.011
Pt-Pt	11.8 ± 2.4	2.709 ± 0.013	113 ± 20	4.3 ± 1.7	
Pt-O	2.0 ± 1.2	2.032 ± 0.034	137 ± 114		
Pt NPs, 4-5 nm					0.002
Pt-Pt	9.4 ± 0.4	2.756 ± 0.002	57 ± 2	7.0 ± 0.5	
Pt foil					0.001
Pt-Pt	12.0 ± 0.1	2.763 ± 0.001	40 ± 1	7.1 ± 0.4	

The PDF data from the leached sample shows that the main structure in the sample is *fcc*, as clear Pt-Pt peaks are apparent. This is illustrated in Figure 4 in the main paper. We see no clear peaks or shoulders from Co-Co (first peak expected at 2.51 Å) or Co-O (first peak expected at 2.1 Å) anywhere in the PDF. This is due to the much higher scattering power of Pt compared to Co, as well as the small content of Co in the

sample (ca. 10%). Considering the linear relationship between atomic number *Z* and the X-ray scattering power of the elements, the ratio between Pt-Pt and Co-Co peaks in the PDF from the sample can be estimated to be $(Z_{Pt}^2*0.9)/(Z_{Co}^2*0.1) = 75$, i.e. the Pt-Pt peaks dominate the PDFs from this sample.

Results from fits of the *fcc* structure are given in Tables S4 and S5, while the fits are shown in the main paper. The scale factor, the cubic unit cell parameter *a* and the crystallite size was refined along with U_{iso} (the Debye-Waller factor) and a parameter taking into account correlated motion, delta2.

Table S4. Results from fit of the Pt fcc structure (space group Fm-3m) over the PDF range from 1-40 Å.

Scale	0.74734
Unit cell parameter a	3.8487 Å
Crystallite size (Spherical model)	24.8 Å
U_{iso} Pt	0.0181 Å^2
Parameter for correlated motion (delta2)	5.01 Å

Table S5. Results from fit of the Pt fcc structure (space group Fm-3m) over the PDF range from 18-40 Å.

Scale	0.699101
Unit cell parameter a	3.830 Å
Crystallite size (Spherical model)	39.1 Å
U_{iso} Pt	0.056 Å^2
Parameter for correlated motion (delta2)	-

In the local range, all major peaks in the experimental PDF can be relatively well fitted with a normal *fcc* structure, although the difference curves show features that have previously been assigned to twinned *fcc* structures[3]. However, the fit results also show that to describe the long-range PDF region, a smaller unit cell parameter and a larger U_{iso} value is required compared to the local region. Fits to several PDF ranges were tested, all showing the same trend.

This effect can be interpreted in terms of the proposed core/shell CoO/Pt nanostructure and curvature in the network bones. Since the PDF is completely dominated by signal from Pt, we only consider the Pt-Pt peaks arising from the suggested structure. In the very local region (r = 1-15 Å), the only significant contribution to the PDF is likely to arise from the Pt shells, and thus appear as a strained Pt nanostructure which can be described through a single *fcc* phase with a small crystallite diameter, confirming the results obtained in EXAFS, TEM and SAXS analysis. However, as seen from the fits, the structural features at higher *r* values can also be described by the *fcc* structure, just with a smaller unit cell and larger U_{iso} parameter. In a core/shell structure, the Pt shell will take a continuous *fcc* structure throughout the bones. If considering the high-r region of the PDF, the main contribution will be Pt-Pt pairs *across* the core of the bones. The presence of the Co or CoO core may reduce the average lattice parameter in the *fcc* structure at these longer distances, which means that the model will refine to smaller lattice parameter values when considering only the high *r*-range. Furthermore, we will no longer see sharp, well defined peaks but much broader features. This is exactly what we observe in terms of the increased U_{iso}-values from high *r* refinements.

Density functional theory (DFT) calculations - Computational details and surface model

Potential energies were calculated using the GPAW[4] software package, where exchange and correlation contributions to the electronic energies were described using the RPBE[5] functional. We used a Monkhorst-Pac[6] sampling of at least 4 x 4 x 1 k points for slabs. Occupation of one-electron states was calculated at an electronic temperature of kBT = 0.1 eV, with all energies extrapolated to T = 0 K. Convergence of structural optimization is reached when the sum of absolute forces acting on the atoms becomes less than 0.05 $eVÅ^{-1}$. The Atomic Simulation Environment (ASE)[7] was used to set up the atomic structures.

As evidenced by XPS results, heat treatment of the Pt-CoO networks leads a change of its electronic properties. The main enhancement of the specific activity cannot be caused by the ligand effect, but is suggested to be caused by a geometric effect of the Cobalt Oxide core on the skin Pt layer on the outside. This effect results in a straining effect which determines adsorption energies. This result allows us to simplify the model by considering only the strained Pt overlayer that is formed on top of cobalt oxide rather than the full system (cobalt oxide + Pt overlayer)[1].

CoO with rock salt structure consists of two interpenetrating *fcc* sublattices of Co^{2+} and O^{2-}. The lattice constant of CoO is 4.260 Å.[8] Under CoO(100) surface with 3.01 Å for the nearest neighbor atomic bond length of Co atoms, both Pt(100) and Pt(111) slab can be constructed when considering nearest neighbor

atomic bond length for Pt-Pt (d_{Pt-Pt}) in EXAFS data fitting (Table S3) which is around 2.71 to 2.73 Å. On the top of Figure S21, d_{Pt-Pt} around 2.72 Å is obtained for both directions on Pt(100) slab, while there is one over-compressed direction (d_{Pt-Pt} = 2.65 Å) for Pt(111) slab compared to the experimental data and d_{Pt-Pt} in the other direction is 2.72 Å on the top of Figure S22.

Firstly, a strained 3 x 3 Pt(100) slab with four layers was used to represent the Pt overlayer. Strained Pt overlayers are represented by periodically repeated slabs separated by at least 10 Å of vacuum. OH molecules were adsorbed in a bridge site. The molecule and top two atomic layers were allowed to relax.

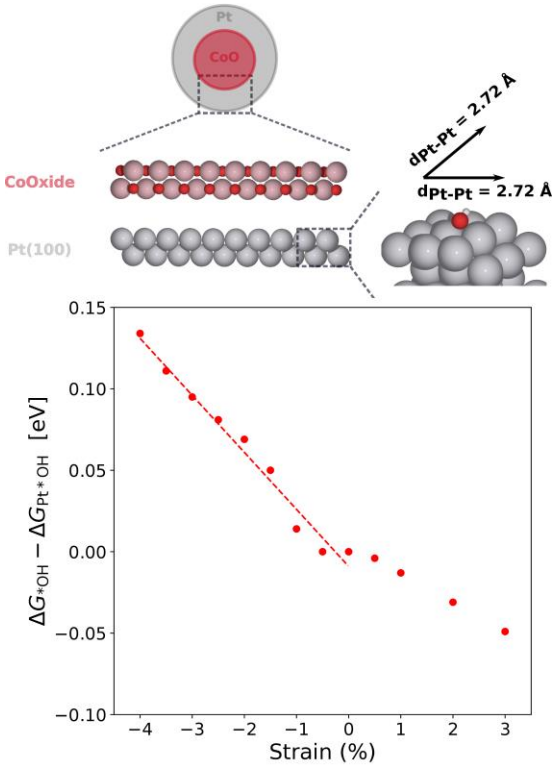

Figure S21. Difference in adsorption energy of OH on Pt(100) as a function of strain from 4% compression to 3% expansion. The binding energies of OH was fitted with a linear regression (shown by the red line) to the in-plane strain yielding a slope of -0.03 eV/% in the region from 0% to -4% strain. The top schematically illustrates the Pt(100) slab over Cobalt Oxides in a core-shell structure.

Besides, a strained 2 x 2 Pt(111) slab with four layers was also used to represent the Pt overlayer which already has been investigated before.[9]

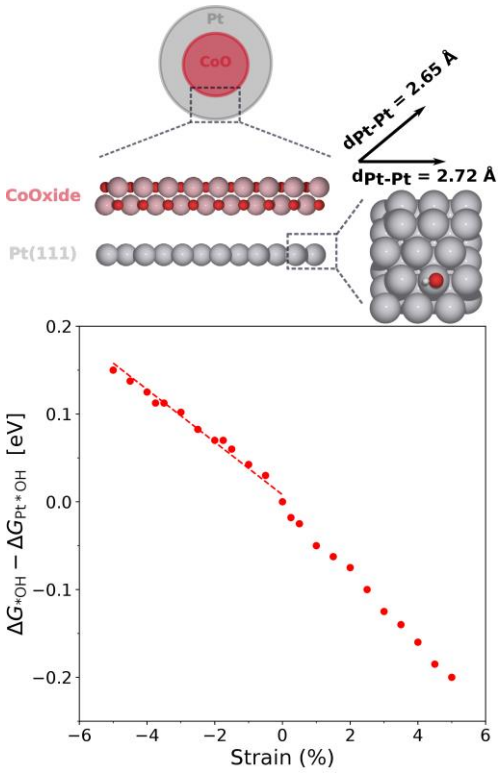

Figure S22. Difference in adsorption energy of OH on Pt(111) as a function of strain from 5% compression to 5% expansion. The binding energies of OH was fitted with a linear regression (shown by the red line) to the in-plane strain yielding a slope of -0.03 eV/% in the region from 0% to -5% strain. (Reproduced from ref 7 copyright © 2016, American Association for the Advancement of Science) The top schematically illustrates the Pt(111) slab over Cobalt Oxides in a core-shell structure.

For calculating relative stabilities, we used the GPAW code in the grid-space mode with a grid density of h = 0.18 Å. We used surface unit cell size (3x3) for Pt(100). Atoms in the two bottom layers are kept fixed to bulk distances, whereby those in remaining layers are allowed to relax in order to assume minimum energy positions. The RPBE relaxed lattice constant of Pt is 3.99 Å. The lattice constant is ca. 2% higher than the experimental value (3.92 Å) because the RPBE functional generally tends to overestimate the lattice parameters at the expense of getting better adsorption energies. Experimental lattice constants have been adjusted to produce the same 2% overestimation as that found for Pt with RPBE.

Strain-activity-reactivity relationships

The binding energies of OH, ΔE_{OH}, were calculated on both an extended Pt(100) and Pt(111) surfaces relative to water and hydrogen in gas phase.

$\Delta E_{OH} = E^*_{OH} - (E_{H2O} - 1/2E_{H2}) - E^*$

where E^* and E^*_{OH} are the energies of a bare Pt slab and Pt with OH adsorbed both for (100) and (111) facets.

Differences in zero-point energy, entropy and solvation energy were included in order to obtain Gibbs free energies (ΔG_{OH}) at room temperature.[10]

$\Delta G_{OH} = \Delta E_{OH} + 0.35\ eV - 0.3\ eV$

As shown in Figure S21 and Figure S22, the trend in ΔG_{OH} is close to linear in the strain below 0% both for Pt(100) and Pt(111), in accordance with expected trends[11]. The linear relationship with the in-plane strain, has a slope of -0.03 eV/% in the region of strain below 0%. According to the core-shell structure described above, the contraction of the bulk d_{Pt-Pt} for Pt-CoO would be 1.28%. As a result, both for Pt(100) and Pt(111) the intrinsic activity on Pt-CoO can be enhanced 38 mV as compared to pure Pt(110) and Pt(111) respectively.

Even though pure Pt(111) slab cannot exactly fit the experimental Pt-Pt distance in both directions, possibly, both Pt(100) and Pt (111) facets coexist in the Pt-CoO since Pt(111) termination is the facet with the lowest surface energy, and thus it is expected to dominate the surface of a polycrystalline sample. Furthermore, due to the intrinsic difference for the adsorption of OH between pure Pt(100) (ΔG_{OH} = 0.64 eV) and pure Pt(111) (ΔG_{OH} = 0.75 eV), Pt(111) will always dominate the overall ORR process when both facets are available.

Measurements in a gas diffusion electrode half-cell.

In order to measure the oxygen reduction reaction under more realistic conditions it is possible to use the gas diffusion electrode half-cell setup. In this setup oxygen mass transport is not limited by the solubility in water but transported directly to the catalytic site as it is the case in the fuel cell.

Therefore, we used the gas diffusion electrode setup which was recently developed[12]. The geometric activity of the support free Pt-CoO catalyst layer is especially promising at room temperature without humidification. At elevated temperatures water management has to be optimized, as it is done for Pt/C for decades.

As it can be seen in the E-I curve for the np Pt-CoO networks the activity at low overpotentials is promising exceeding the geometric activity of dry Pt/C. The data for Pt/C is taken from literature and was done with the same setup and the same conditions. It can be seen that the higher specific activity and surface area is increasing the activity in the gas diffusion electrode until 0.6 V_{RHE}. Below 0.6 V_{RHE} the activity decreases due to mass transport issues but is still higher compared to Pt/C under these conditions.

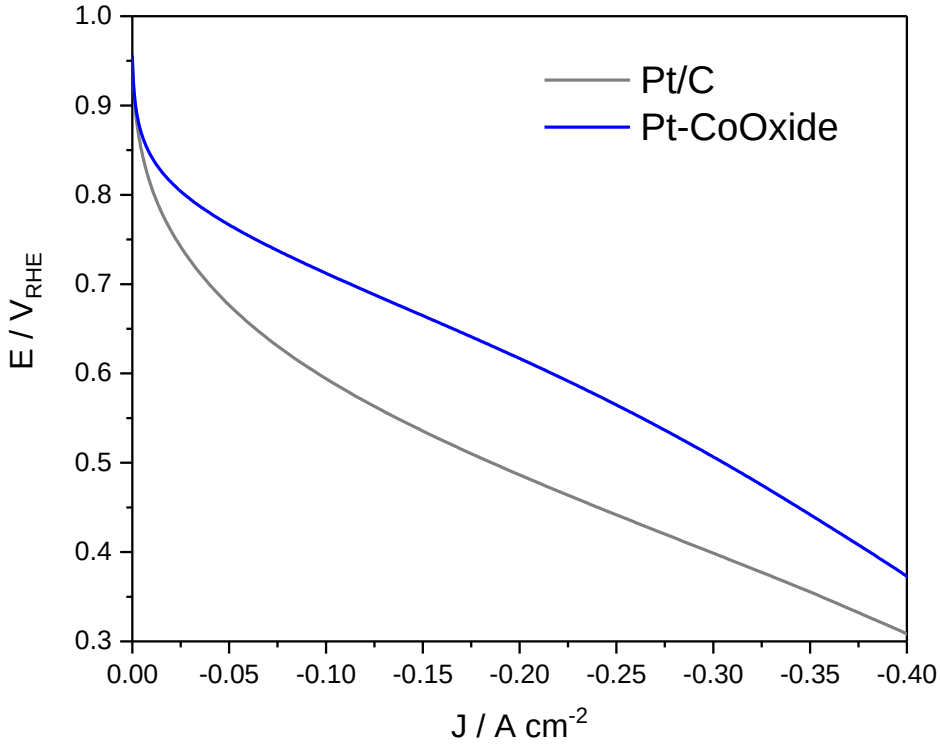

Figure S23. Measurements of the np Pt-CoO network in the gas diffusion electrode half-cell setup. The conditions were chosen as previously published and the data for Pt/C are taken from this reference[12]*. Therefore the catalyst layer was deposited onto SGL BC39 and measured in 4 M HClO4, 50 mV* s^{-1} *at room temperature, with membrane (Nafion 117) and without humidification of the pure oxygen. As reference electrode a trapped hydrogen reference electrode was used. The potential was verified before and after measuring the activity.*

In situ potential-dependent EXAFS

Figure 3b in the main paper shows the ratios from the potential-resolved partial coordination numbers (N) of Pt-O and Pt-Pt for np-PtCo during ORR based from *in situ* EXAFS analysis. It is noted that the EXAFS data were analyzed by assuming that the nanoporous Pt films do not contain or show at least very negligible content of cobalt. To illustrate the meaning of this experiment, 30 wt. % Pt/C was taken as a reference material. First, for 30 wt. % Pt/C the ratio of N(Pt-O)/N(Pt-Pt) changes drastically at potentials of above 0.8 V_{RHE} and continuously increases in the anodic scan. This observation is not surprising because of the formation of oxygen monolayer at the Pt surface stemmed from the oxidation of water above 0.8 V_{RHE}. This process is reversible because during the cathodic scan the N(Pt-O)/N(Pt-Pt) ratio drops back to the previous value at 0.5 V_{RHE}, where typically the double layer region of Pt appears. This behavior is more pronounced by decreasing the particle size of Pt nanoparticles as the number of surface atoms in respect of bulk atoms increases. Very interestingly, the np Pt-CoO shows almost no changes in the N(Pt-O)/N(Pt-Pt) ratios as a function of the applied potential. It is noted that the ligaments of np Pt-CoO are in nanometer size, similar to the particle size of 30wt.% Pt/C. This remarkable observation can be explained by the linking of the ligaments of np Pt-CoO forming a macroscopic network. Due to its network structure, the Pt-CoO shows similar properties of a polycrystalline Pt surface.

References

1. Stephens, I. I. E. L. L. *et al.* Understanding the electrocatalysis of oxygen reduction on platinum and its alloys. *Energy Environ. Sci.* **5,** 6744–6762 (2012).

2. Mayrhofer, K. *et al.* Measurement of oxygen reduction activities via the rotating disc electrode method: From Pt model surfaces to carbon-supported high surface area catalysts. *Electrochim. Acta* **53,** 3181–3188 (2008).

3. Banerjee, S. *et al.* Improved Models for Metallic Nanoparticle Cores from Atomic Pair Distribution Function (PDF) Analysis. *J. Phys. Chem. C* **122,** 29498–29506 (2018).

4. Mortensen, J. J., Hansen, L. B. & Jacobsen, K. W. Real-space grid implementation of the projector augmented wave method. *Phys. Rev. B - Condens. Matter Mater. Phys.* **71,** 1–11 (2005).

5. Hammer, B., Hansen, L. B. & Nørskov, J. K. Improved adsorption energetics within density-functional theory using revised Perdew-Burke-Ernzerhof functionals. *Phys. Rev. B - Condens. Matter Mater. Phys.* **59,** 7413–7421 (1999).

6. Pack, J. D. & Monkhorst, H. J. Special points for Brillouin-zone integrations. *Phys. Rev. B* **16,** 1748–1749 (1977).

7. Bahn, S. R. & Jacobsen, K. W. An object-oriented scripting interface to a legacy electronic structure code. *Comput. Sci. Eng.* **4,** 56–66 (2002).

8. Kannan, R. & Seehra, M. S. Percolation effects and magnetic properties of the randomly diluted fcc system CoMgO. **35,** 6847–6853 (1987).

9. Escudero-Escribano, M. *et al.* Tuning the activity of Pt alloy electrocatalysts by means of the lanthanide contraction. *Science (80-.).* **352,** 73–76 (2016).

10. Nørskov, J. K. *et al.* Origin of the overpotential for oxygen reduction at a fuel-cell cathode. *J. Phys. Chem. B* **108,** 17886–17892 (2004).

11. Mavrikakis, M., Hammer, B. & Nørskov, J. K. Effect of strain on the reactivity of metal surfaces. *Phys. Rev. Lett.* **81,** 2819–2822 (1998).

12. Inaba, M. *et al.* Benchmarking high surface area electrocatalysts in a gas diffusion electrode: measurement of oxygen reduction activities under realistic conditions. *Energy Environ. Sci.* **11,** 988–994 (2018).